

Sky-TCAM: Low-Power Skyrmion-Based Ternary Content Addressable Memory

Ruifu Zhang[®], Chunli Tang[®], *Student Member, IEEE*, Xiaozhen Sun, Mengyuan Li, *Student Member, IEEE*, Wencan Jin, Peng Li[®], *Member, IEEE*, Xiaomin Cheng, and X. Sharon Hu[®], *Fellow, IEEE*

memories Abstract— Low-cost content-addressable (CAMs) are highly desirable for many applications where high-speed search is needed such as network routers and machine learning. We propose a low-power, compact, fast magnetic skyrmion-based ternary CAM (Sky-TCAM) cell design. Each cell comprises a 5T2R structure with five transistors and two magnetic tunnel junctions (MTJs). The search current polarity together with the stored bit can realize the XOR logic. When a mismatch happens, the skyrmion appears beneath one MTJ, leading to the discharge of the matchline (ML). While the search energy-delay-product (EDP) is comparable with that of non-volatile (NV) ternary CAMs (TCAMs), Sky-TCAM shows the lowest EDP of 8.74 \times $10^{-25}~J\cdot s$ among all TCAMs we compare. Our research shows that Sky-TCAM is promising for building low-power and low-latency computation applications.

Index Terms—Content-addressable memories (CAMs), magnetic tunnel junction (MTJ), skyrmion, spintronic logic.

I. INTRODUCTION

A CONTENT addressable memory (CAM) is an associative memory that searches by content as opposed to searching by address. A ternary CAM (TCAM) supports data

Manuscript received 4 April 2023; accepted 4 May 2023. Date of publication 18 May 2023; date of current version 21 June 2023. The work of Chunli Tang was supported by the Alabama Graduate Research Scholars Program (GRSP) funded through the Alabama Commission for Higher Education and administered by the Alabama EPSCoR. The work of Mengyuan Li and X. Sharon Hu was supported in part by Al Chip Center for Emerging Smart Systems (ACCESS) sponsored by InnoHK funding, Hong Kong SAR. The work of Wencan Jin was supported in part by NSF EPM under Grant DMR-2129879 and in part by the Auburn University Intramural Grants Program. The review of this article was arranged by Editor N. Xu. (Ruifu Zhang, Chunli Tang, Xiaozhen Sun, and Mengyuan Li contributed equally to this work.) (Corresponding authors: Wencan Jin; Peng Li; Xiaomin Cheng; X. Sharon Hu.)

Ruifu Zhang and Xiaomin Cheng are with the School of Integrated Circuits, Huazhong University of Science and Technology, Wuhan 430074, China (e-mail: xmcheng@mail.hust.edu.cn).

Chunli Tang is with the Department of Electrical and Computer Engineering, Auburn University, Auburn, AL 36849 USA.

Xiaozhen Sun and Peng Li are with the School of Microelectronics, University of Science and Technology of China, Hefei, Anhui 230026, China (e-mail: lipeng18@ustc.edu.cn).

Mengyuan Li and X. Sharon Hu are with the Department of Computer Science and Engineering, University of Notre Dame, Notre Dame, IN 46556 USA (e-mail: shu@nd.edu).

Wencan Jin is with the Department of Physics and Department of Electrical and Computer Engineering, Auburn University, Auburn, AL 36849 USA (e-mail: wjin@auburn.edu).

Color versions of one or more figures in this article are available at https://doi.org/10.1109/TED.2023.3274506.

Digital Object Identifier 10.1109/TED.2023.3274506

bits having the "don't care" state, in addition to "0" and "1" [1]. TCAM has been widely used in network routers, database searches, etc. The rapid increase in data analytics and machine learning workloads, such as in nearest neighbor search and memory-augmented neural networks for few-shot learning problems [2], demands scalable and more energy-efficient TCAMs. TCAM arrays built with CMOS transistors suffer from high power and low density, thus limiting their adoption [2]. The advancement of non-volatile (NV) memory technologies, such as ferroelectric FETs, resistive random access memories (RRAMs), and spintronic RAMs, open new directions for TCAM designs due to their advantages of low power, higher density, zero leakage current, and new functionalities [1], [2], [3], [4], [5].

Spintronic devices have attracted attention for novel memory-based computing devices [2]. Several CAM and TCAM designs based on magnetic tunnel junctions (MTJs) and magnetic domain walls have been proposed and demonstrated. They have the potential to outperform CMOS TCAMs in power consumption and integration density. However, those proposed designs have a high write power consumption or rely heavily on the use of multiple CMOS transistors (e.g., six or more transistors) in the TCAM cell [2]. In this regard, new CAM/TCAM designs that can fully exploit the unique advantages of recently discovered spintronic physics should be studied.

Skyrmion is a magnetic vortex structure protected by topology. They arise from the competition between Dzyaloshinskii'Moriya interaction (DMI) and perpendicular anisotropy energy interactions. Skyrmions have many unique properties, including nanometer diameter, topological stability at room temperature, and current-controlled motion. These unique characteristics enable skyrmion the potential to be an ideal candidate for novel memory applications, where it can carry information bit "0" and bit "1." There are already new devices utilizing skyrmions, such as skyrmion logic gates [6], skyrmion racetrack memories [7], and skyrmion artificial neural network systems [8], [9], [10]. Using the conventional CMOS architecture, the skyrmion-based logic gates can achieve unique functionalities with better performance compared to CMOS-only hardware designs [11].

Skyrmion has been proposed to realize the CAM function, however, it does not store bits in the device; moreover, the search energy-delay-product (EDP) is high [12]. In this work, we propose a compact, fast, and low-power skyrmion-

based ternary CAM (Sky-TCAM) cell design combined with CMOS circuits. The Sky-TCAM uses a five transistor/two MTJ structure, which is more compact than the state-of-theart spin transfer-torque (STT) TCAM design (e.g., [2]). Sky-TCAM achieves a write time of 0.85 ns, write EDPs of $8.74 \times 10^{-25} \text{ J} \cdot \text{s}$, search time of 179 ps, and search EDPs of $3.01 \times 10^{-24} \text{ J} \cdot \text{s}$. Sky-TCAM improves the write EDPs by four orders of magnitude compared with the most advanced STTRAM-TCAM (2.8 \times 10⁻²¹ J \cdot s). Among the emerging memory technologies, the Sky-TCAM design shows ultralow write EDP, while the search EDP is comparable with that of the TCAMs based on NV memories. In the following, we first introduce the Sky-TCAM cell structure and operation. Then, we study the impact of geometric and magnetic parameters on the writing operation of the Sky-TCAM. Finally, we present the search energy, delay, and EDP evaluations.

II. SKY-TCAM

In this section, we first present our novel Sky-TCAM device and cell design, then discuss the Sky-TCAM operation.

A. Sky-TCAM Device and Cell

The device structure is shown in Fig. 1. Sky-TCAM comprises a nanotrack made of a perpendicular magnetic anisotropy (PMA) layer/heavy metal (HM) film stack, as well as two MTJs. MTJ is a sandwich structure consisting of two ferromagnetic layers separated by a thin dielectric layer. Electrons can be polarized and tunnel through the dielectric layer thus showing magnetoresistance (MR). The tunneling MR depends on whether the magnetization of the two ferromagnetic layers is parallel or anti-parallel, which results in low and high MR, respectively. The corresponding tunneling MR ratio TMR = $(G_P - G_{AP})/G_{AP}$. They usually work as detectors for skyrmions in spintronic devices. In this case, one ferromagnetic layer has fixed magnetization (reference layer), and as a skyrmion passes the nanotrack under the dielectric layer (working as a free layer), the magnetization of the nanotrack changes thus the MTJ shows a different MR. After Sky-TCAM is fabricated, a skyrmion is injected into the nanotrack and there is no need to regenerate during the working operations because of its nonvolatility. When current flows in the nanotrack, it generates a spin-orbit torque (SOT) which can drive the skyrmion to move in the nanotrack. The dark red section in the center of the nanotrack works as a skyrmion barrier with a higher PMA $K_{u,BR}$ than the rest of the nanotrack. The barrier imposes a current threshold Jth, and the applied current must exceed Jth to drive the skyrmion across the barrier. Utilizing the skyrmion-edge repulsion effect, we have designed a unique nanotrack with quadruple notches. The structure has three functionalities: first, it constrains the skyrmion to move within the central region of the nanotrack with a short travel time; second, it induces a small threshold current Jth for driving the skyrmion motion; third, the paired notches prevent the skyrmion from annihilating close to the notches. The MTJs on top of the nanotrack work as the skyrmion detectors. When the skyrmion reaches underneath one MTJ, the MTJ exhibits a low MR (e.g., $8 \text{ k}\Omega$); otherwise,

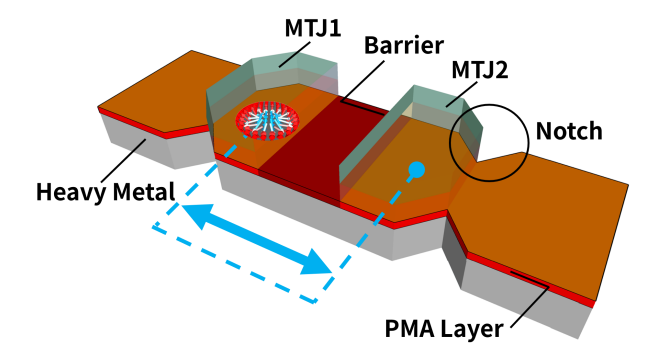


Fig. 1. Three-dimensional structure of a Sky-TACM device. From top to bottom: green for MTJ1 and MTJ2; red for magnet layer with perpendicular magnetic anisotropy (PMA layer); the dark red region in the PMA layer indicates a barrier that has a different PMA strength; the skyrmion is located underneath MTJ1 and can move in the nanotrack.

TABLE I
OPERATION OF SKY-TCAM CELL

	WR	WR	WL	SL	SL	SrL	skyrmion Pos.
Write"0"	$V_{ m write}$	0	$V_{\rm dd}$	0	0	0	Right
Write"1"	0	$V_{ m write}$	$V_{\rm dd}$	0	0	0	Left
Write"X"	$V_{ m write}/0$	$V_{ m write}/0$	$V_{ m dd}$	0	0	0	Right/Left
Search"0"	0	0	0	0	$V_{\rm dd}$	0	/
Search"1"	0	0	0	V_{dd}	0	0	/
Search"X"	0	0	0	0	0	0	/

MTJ remains a high MR (e.g., 18 k Ω) [2]. The location of the skyrmion in the nanotrack represents different stored bit information. Bit "1" is stored when the skyrmion is between the skyrmion barrier and the two notches on the left side, as indicated in Fig. 1. Similarly, Bit "0" is stored when the skyrmion is on the right side. Current induced SOT changes the location of the skyrmion, thus flipping the bit information that the TCAM cell stores.

We adopt the NOR type TCAM design as shown in Fig. 2(a), where a row of TCAM cells is connected to the matchline (ML) in parallel. A precharge circuitry controls the precharging of the ML. Fig. 2(b) shows the circuit schematic of the Sky-TCAM cell that consists of one Sky-TCAM device and five transistors. The left end of nanotrack is connected to the transistor T_5 that controls the writing current from WR and $\overline{\text{WR}}$ through WL. The nanotrack resistances are R_n (n=1–5). The two MTJs (R_{MTJ1} , R_{MTJ2}) on top of the nanotrack are connected to ML through T_1 – T_4 transistors. T_1 , T_2 form the controlled discharge paths for ML, and the drains of T_3 and T_4 are connected to the search lines (SL, $\overline{\text{SL}}$) where the input query is provided.

B. Sky-TCAM Operation

Table I summarizes the TCAM write and search operations. To write "0" to a cell, $V_{\rm write}$ is applied to WR, "1" is applied to WL, and "0" is applied to $\overline{\rm WR}$ as well as the source line (SrL). If the write current $J_{\rm write} \geq$ the threshold current $J_{\rm th}$, a powerful SOT is generated, which drives the skyrmion to enter and cross the barrier (dark red region of the nanotrack) and eventually reach the right notches of the nanotrack. Similarly, the writing "1" process sets the skyrmion to the left side. To write the "don't care" state, either the process for writing "0" or "1" can be used.

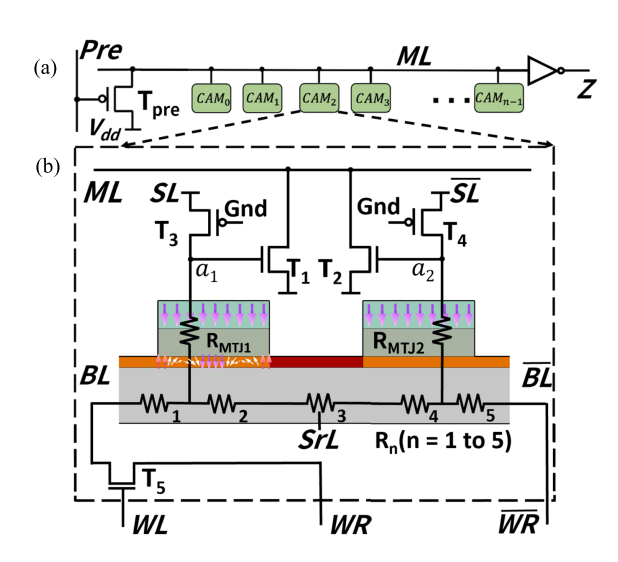


Fig. 2. (a) Representative row of a Sky-TCAM array based on NOR connection of n CAM cells. $T_{\rm Pre}$ is the transistor through which the pre signal precharges ML. (b) Circuit schematic of the Sky-TCAM cell. BL/BL: bitlines; SL/SL: searchlines; T_1 and T_2 are nMOS transistors connected to ML. T_3 and T_4 are pMOS transistors that are always on. T_5 controls the writing current from WR and $\overline{\rm WR}$. $R_{\rm MTJ1}$ and $R_{\rm MTJ2}$ represent the resistance of MTJ 1 and 2. R_n (n=1 to 5) represent resistances of different parts of the nanotrack.

During the search process, ML is first precharged to $V_{\rm dd}$ by turning on the precharge transistor $T_{\rm pre}$ in Fig. 2(a). To search for "1," $V_{\rm dd}$ is applied to SL and ground (GND) to $\overline{\rm SL}$. If the skyrmion is at the right side of the nanotrack ("0" is stored), $R_{\rm MTJ1}$ has a high resistance, and $R_{\rm MTJ2}$ has a low resistance. R_1 to R_5 , T_1 and T_3 are chosen such that node a_1 exhibits a high voltage V_h , which turns on transistor T_1 and discharges ML. Meanwhile, T_2 keeps being turned off. This demonstrates a mismatch. Otherwise, if the skyrmion is at the left side of the nanotrack ("1" is stored), the resistance of $R_{\rm MTJ1}$ is low and $R_{\rm MTJ2}$ is high. A relative low voltage V_1 is measured at node a_1 , which turns off T_1 , while T_2 remains off. This leads to ML keeping high, indicating a match.

III. WRITING OPERATION IN SKY-TCAM

This section discusses the skyrmion-TCAM device writing performance. Specifically, we study the impacts of damping constant α , current density J, magnetic anisotropy (both nanotrack $K_{u,\text{NT}}$ and barrier $K_{u,\text{BR}}$), and the barrier width, on the device performance and stability.

A. Demonstration of the Writing Process

Fig. 3 shows the dynamic behavior of the Sky-TCAM device in the writing and searching process. Fig. 3(a) and (b) are snapshots during writing "0" with the stored state being "0" and "1," respectively. In Fig. 3(a), the stored bit is "0," while the bit to be written is also "0." A left-to-right writing current $J \geq$ threshold J_{th} flows in the nanotrack and drives the skyrmion rightward; the two notches at the right side stop the skyrmion from moving past them because of the skyrmion-notch repulsion. In this regard, the skyrmion relaxes and returns to its original place, and stabilizes at the right side

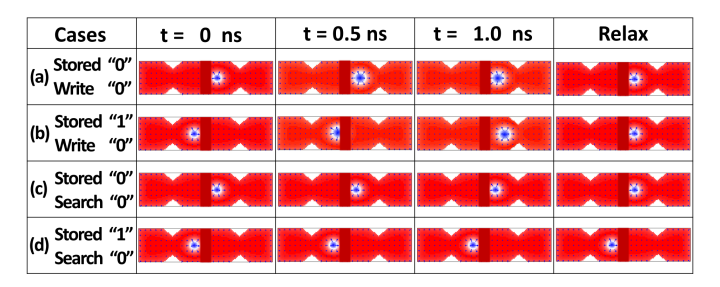


Fig. 3. Micromagnetic simulations for writing and searching process. For the most optimized device performance, we set nanotrack PMA $K_{u,\rm NT}=8.5\times10^5~\rm J/m^2$, barrier PMA $K_{u,\rm BR}=9.0\times10^5~\rm J/m^2$, writing current $J=6\times10^{10}~\rm A/m^2$, and barrier width is 10 nm. During the searching process, the skyrmion position remains unchanged because no current is induced in the nanotrack.

of the barrier underneath MTJ2. Thus, the stored bit stays at "0." In Fig. 3(b), the stored bit is "1," and a left-to-right writing current drives the skyrmion to cross the barrier and reach the right side of the nanotrack. Due to the repulsion of the two notches, the skyrmion relaxes and stabilizes underneath MTJ2, representing bit "1."

B. Optimization of Writing Process

We study the effect of different parameters on the device writing operations. For the micromagnetic simulations in this article, We use object-oriented micromagnetic framework (OOMMF), a public micromagnetics program developed at the National Institute of Standards and Technology [13]. Table II summarizes the parameters used in the simulations. The current-induced skyrmion motion is modeled by the Landau–Lifshitz–Gilbert (LLG) equation [14] with SOT terms T as shown below

$$\frac{d\mathbf{m}}{dt} = -\gamma \mathbf{m} \times \mathbf{B}_{\text{eff}} + \alpha \mathbf{m} \times \frac{d\mathbf{m}}{dt} + \mathbf{T}$$
 (1)

$$\mathbf{T} = \tau_{\mathrm{FL}} \mathbf{m} \times \zeta + \tau_{\mathrm{DL}} \mathbf{m} \times (\mathbf{m} \times \zeta) \tag{2}$$

where γ is the gyromagnetic ratio, $\mathbf{B}_{\rm eff}$ is the effective field, which is defined as the derivative of the magnetic energy density ε with respect to magnetization \mathbf{M} ($\mathbf{B}_{\rm eff} = -\delta \varepsilon/\delta \mathbf{M}$), α is the Gilbert damping constant, \mathbf{m} is the magnetization unit vector. The saturation magnetization \mathbf{M}_s , spin Hall angle θ_A and other constants decide $\tau_{\rm FL}$ and $\tau_{\rm DL}$, the coefficients of field-like torque and damping-like torque [15]. ζ is a unit vector determined by the charge-spin conversion process induced by spin-orbit coupling and changes with the current direction. In our simulation, we consider an interfacial DMI at the HM/PMA magnet interface. The corresponding DMI extension module has been added to the OOMMF software [16].

Fig. 4(a) shows the dependence of the Sky-TCAM device operation on the current density J and the damping constant α . The green circles indicate that the skyrmion can pass the central barrier under the given J and α values. On the contrary, the red circles show that the skyrmion is blocked by the barrier. The nanotrack magnetic anisotropy is set to $K_{u,NT} = 8.0 \times 10^5 \text{ J/m}^2$ and the barrier anisotropy is set to $K_{u,BR} = 8.5 \times 10^5 \text{ J/m}^2$. From the data, we can draw the following conclusions: 1) our proposed design can work with a large range of α from 0.05 to 0.25 with a suitable

TABLE II
SIMULATION PARAMETERS FOR SIMULATING THE DYNAMIC BEHAVIORS
OF SKYRMION

Parameter	Value
Gilbert damping factor α [17]	0.1
Spin Hall angle θ_A [18]	0.4
Saturation magnetization M _s [19]	$5.8 \times 10^5 \text{ A/m}$
DMI constant D [20]	3.5 mJ/m^2
Exchange stiffness A _{ex} [17]	$15 \times 10^{-12} \text{ J/m}$
PMA (Racetrack) K _{u,NT} [17]	$8 \times 10^5 \text{ J/m}^2$
PMA(Barrier) K _{u,BR} [17]	$8.5 \times 10^5 \text{ J/m}^2$
Mesh Size	$1 \text{ nm} \times 1 \text{ nm} \times 1 \text{ nm}$
Device Size	$128 \text{ nm} \times 32 \text{ nm} \times 6 \text{ nm}$
Thickness (PMA)	1 nm
Thickness (Heavy Metal)	5 nm
Resistivity (PMA) [21]	$1.50 \times 10^{-7} \ \Omega \cdot m$
Resistivity (Heavy Metal) [21]	$1.06 \times 10^{-7} \Omega \cdot m$

current density of 2×10^{10} A/m² to 5×10^{10} A/m²; 2) at low α , large current density annihilates the skyrmion, resulting in device operation failure. At high α , a larger current is needed to push the skyrmion passing the barrier, hence increasing the power consumption; and 3) we conclude that $\alpha = 0.1$ gives the best writing and search performance, thus, in the rest of the simulations, $\alpha = 0.1$ is used.

Second, we study the dependence of the skyrmion velocity on the nanotrack PMA $K_{u,NT}$, current density J, and damping constant α . The results are presented in Fig. 4(b). One can see that: 1) the fastest skyrmion velocity of 41 m/s can be achieved at $K_{u,NT} = 8.2 \times 10^5$ J/m², $\alpha = 0.05$, $J = 2 \times 10^{10}$ A/m²; and 2) a faster skyrmion velocity can be acquired at higher $K_{u,NT}$, larger J, and lower α . Moreover, the barrier PMA $K_{u,BR}$ plays a more dominant role in the movement of skyrmion. Higher $K_{u,BR}$ can slow down the skyrmion and even prohibits the skyrmion from crossing the barrier, as is further discussed in Fig. 4(c).

Third, we study the working range of our device with different barrier PMA $K_{u,BR}$, nanotrack PMA $K_{u,NT}$, and barrier widths for the writing operation. We fix the current density at $J = 6 \times 10^{10} \text{ A/m}^2$ for the simulations in Fig. 4(c). Our results in Fig. 4(c) suggest that: 1) for a given $K_{u,NT}$, a bigger difference between $K_{u,BR}$ and $K_{u,NT}$ allows the barrier to block the skyrmion more effectively. Only within a certain range of $K_{u,BR}$ can the device work properly. The smallest value of $K_{u,BR}$ must exceed $K_{u,NT}$ by about 2×10^4 A/m² to ensure that the skyrmion is blocked by the barrier when no current is applied. The difference between $K_{u,BR}$ and $K_{u,NT}$ should not be too large, otherwise it would be too hard for the skyrmion to pass the barrier; 2) the wider the barrier is, the harder it is for the skyrmion to pass the barrier under the same driving current. Thus, the working parameters ($K_{u,BR}$ and $K_{u,NT}$) are narrower for wider barrier under the same $K_{u,NT}$ [see Fig. 4(c)]; and 3) we further notice that when the barrier width is set to 15 nm and $K_{u,NT}$ is set to 7.75×10^5 J/m², the device can still perform the writing operation properly, which is not the case for 5 or 10 nm barrier width. This is because when the barrier is at 15 nm, it can stabilize a skyrmion when $K_{u,NT} \leq 8 \times 10^5 \text{ A/m}^2$.

To further study the influence of the barrier width, we run simulations to identify the threshold current density and

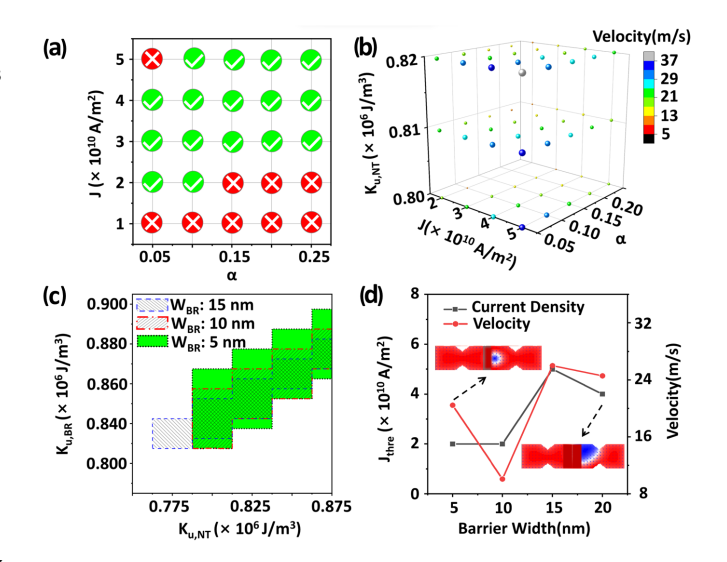


Fig. 4. Device performance of the Sky-TCAM device. (a) Device working range for the current density and the damping constant. (b) Dependence of the skyrmion velocity on the current density, nanotrack PMA, and damping constant. (c) Device working range for barrier PMA, nanotrack PMA, and barrier width. (d) Dependence of threshold current density and skyrmion velocity on barrier width.

TABLE III
WRITE TIME AND POWER CONSUMPTION OF SKY-TCAM AND OTHER
CAM DESIGNS

CAM design	Time (ns)	Energy/bit (fJ)	EDP(J·s)
SOT-TCAM(64-row) [22]	2.4	146	3.50×10^{-22}
ME-TCAM(64-row) [22]	1.8	2.14	3.85×10^{-24}
SRAM-TCAM(64-row) [23]	1	23.6	2.36×10^{-23}
FeFET-TCAM(64-row) [23]	10	2.85	2.85×10^{-23}
STTRAM-TCAM [2]	4	690	2.76×10^{-21}
Sky-TCAM	0.85	1.49	8.74×10^{-25}

skyrmion velocity at different barrier widths. Fig. 4(d) shows that the threshold current density Jth becomes higher as barrier width increases because of the stronger barrier. From Fig. 4(c) and (d), we can conclude that the device works best at a 10 nm barrier width. If the barrier is narrower, the skyrmion is located too close to the center of the nanotrack, which makes it hard to be detected and distinguished by the two MTJs. If the barrier is wider, the skyrmion is easily broken at the edge of the device, and the device's working range of J is restricted.

To summarize, the values of the design parameters including J, barrier width, $K_{u,BR}$ and $K_{u,NT}$ must be carefully chosen so that the tradeoff between power consumption and device stability can be well optimized. We choose $K_{u,NT} = 8.5 \times 10^5 \text{ J/m}^2$, $K_{u,BR} = 9.0 \times 10^5 \text{ J/m}^2$, writing current $J = 6 \times 10^{10} \text{ A/m}^2$, and barrier width 10 nm. By performing the circuit model simulations including T_5 and the nanotrack, these parameters yield the lowest writing EDP of $8.74 \times 10^{-25} \text{ J} \cdot \text{s}$ among all the TCAMs as shown in Table III.

IV. SEARCH PERFORMANCE OF SKY-TCAM

In this section, we use a resistive circuit model extracted from our device of the Sky-TCAM cell to evaluate the proposed Sky-TCAM circuit (see Fig. 2) and compare it with the skyrmion-based TCAM cell, STT CAM, RRAM CAM, STTRAM-TCAM design in terms of latency and power.

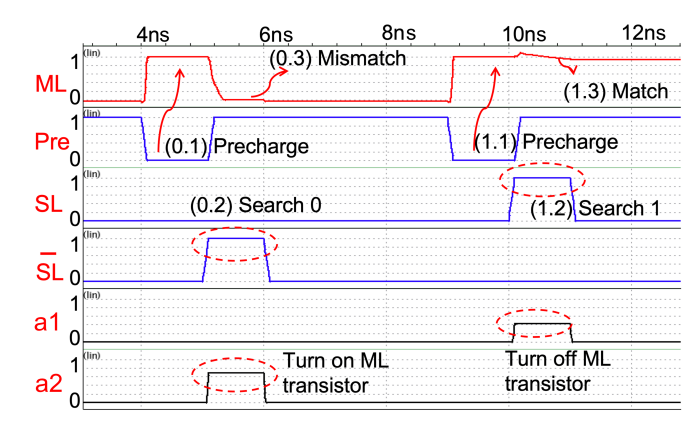


Fig. 5. Voltage waveforms of different nodes in Sky-TCAM circuit simulation. Searching for "1" and "0" are performed while "1" is stored in the TCAM cell. 0–8 ns: search for "0," 8–12 ns: search for "1." (0.1), (0.2), (0.3), (1.1), (1.2), (1.3) represent the order of the operations.

To obtain the search performance of the Sky-TCAM cell, we build a circuit model [see Fig. 2(b)] for the nanotrack and MTJ and use HSPICE for simulations. The 22 nm predictive technology model (PTM) [24] is adopted for circuit implementation. We use TMR = 125% with parallel MTJ resistance of 8 k Ω and antiparallel of 18 k Ω . These MTJ resistances are consistent with those in [2]. The width of T_3 and T_4 are set to 200 nm to match the resistances of two MTJs. R_1 – R_5 in Fig. 2 are calculated according to the geometry of the nanotrack and material resistivities as shown in Table II.

A. Demonstration of Searching Process

Fig. 3(c) and (d) are snapshots during the search process. T_5 is turned off by WL, and WR, $\overline{\text{WR}}$ are set to 0, therefore no current flows in the nanotrack. Fig. 3(c) shows the case that the stored bit "0" matches the input query bit. During the searching process, MTJ2 remains at a low MR, and T_2 is closed. Meanwhile, T_1 is also closed because SL is set to "0." As a result, ML remains a high voltage. On the other hand, Fig. 3(d) shows that the stored bit "1" and the searching signal "0" have a mismatch. In this regard, MTJ2 shows a high MR, thus opening T_2 and discharging ML while T_1 remains closed.

Fig. 5 shows the input and output voltage waveforms during the search operations in Sky-TCAM. Bit "1" is stored in the device initially and ML is charged to $V_{\rm dd}$ by the Pre signals. The input query "0" and "1" are applied sequentially through SL/ $\overline{\rm SL}$. During the search for "0" (0–8 ns), ML is pulled to low by transistor T_2 and outputs a mismatch. During the search for "1" (8–16 ns), ML remains high and outputs a match. The waveform of a_1 and a_2 are also shown in Fig. 5 which dictates the states of transistors T_1 and T_2 .

B. Search Performance and Comparison

We simulate the proposed Sky-TCAM cell with the HSPICE simulations, which achieves a search power of 17.2 fJ/bit, and a search latency of 179 ps. The supply voltage is set to 1 V in the simulation. Table IV compares the search energy, latency, and EDP of the Sky-TCAM design and other types of TCAM cells design [2]. The search EDP is comparable with other types of TCAM cells [12].

TABLE IV
SEARCH LATENCY AND POWER CONSUMPTION OF SKY-TCAM AND
OTHER CAM DESIGNS

GANGE:	T . ()	T # '- (CT)	EDD (I)
CAM design	Latency (ns)	Energy/bit (fJ)	EDP (J·s)
STT CAM-1 [25]	0.2	37.37	3.50×10^{-22}
STT CAM-2 [26]	0.17	0.17	2.89×10^{-26}
RRAM CAM [27]	2.3	0.18	4.14×10^{-25}
STTRAM-	0.26	4.7	1.22×10^{-24}
TCAM [2]	0.20	4.7	1.22 × 10
Skyrmion-	3.3	10.5	3.47×10^{-23}
CAM cell [12]		10.5	3.47 × 10
Sky-TCAM	0.18	17.2	3.01×10^{-24}

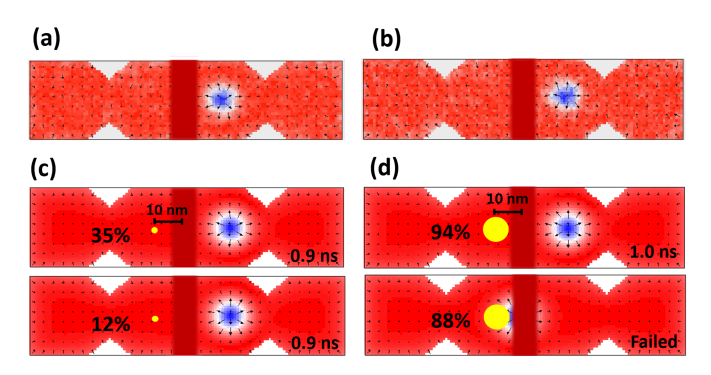


Fig. 6. Effect of temperature and defects. (a) Highest working temperature is 105 K for the default simulation parameters at 0 K. (b) Increment of current density, anisotropy, and DMI constant will raise the working temperature to 200 K. (c) and (d) Magnetic simulations for the writing process with different skyrmion pinning areas. The yellow dots represent the diameter ($D_{\rm pn}$) and position of the pinning sites. The percentage shows the ratio between pinning site PMA $K_{u,\rm pn}$ and nanotrack PMA $K_{u,\rm NT}$ (8.5 × 10⁵ J/m²). The time stands for the time of the writing process. "Failed" means Sky-TCAM cannot work.

V. Effect of Temperature and Defect

In this section, we consider the effects of temperature [28] and defects on the spin dynamics of Sky-TCAM. Fig. 6(a) and (b) show the effect of temperature. Higher temperature affects the size and shape of skyrmion significantly. Sky-TCAM can be functional up to 105 K with the default parameters used elsewhere. After some parameters are properly adjusted, it is possible for it to be functional up to 200 K. Fig. 6(c) and (d) show the effect of defects. Defects induce the skyrmion pinning effect that alters the energy landscape and attracts the skyrmion to move toward the pinning site, leading to device failure [29]. We consider the case that the pinning site has lower PMA than that elsewhere in the nanotrack. The results show that Sky-TCAM can be functional with small-size (2 nm) defects but not large (8 nm) ones.

VI. CONCLUSION

In this work, we have proposed the Sky-TCAM cell and the peripheral circuit. Each TCAM cell comprises a 5T2R structure with five transistors and two MTJs, which is more compact than the state-of-art STTRAM-TCAM. The Sky-TCAM design yields an ultralow-power writing EDP of 8.74×10^{-25} J · s, which outperforms the STTRAM-TCAM significantly. The equivalent circuit simulations suggest that the search energy is comparable with that of other types of TCAMs. Our work has demonstrated that the Sky-TCAM has

the unique benefits of being compact, low-power, and lowlatency, highlighting spintronics as a promising technology to build future electronic devices.

ACKNOWLEDGMENT

Xiaozhen Sun and Peng Li would like to thank the Information Science Laboratory Center, USTC, Hefei, China, for the hardware/software services.

REFERENCES

- R. Karam, R. Puri, S. Ghosh, and S. Bhunia, "Emerging trends in design and applications of memory-based computing and contentaddressable memories," *Proc. IEEE*, vol. 103, no. 8, pp. 1311–1330, Aug. 2015.
- [2] R. Govindaraj and S. Ghosh, "Design and analysis of STTRAM-based ternary content addressable memory cell," ACM J. Emerg. Technol. Comput. Syst., vol. 13, no. 4, pp. 1–22, May 2017.
- [3] L. Tong et al., "2D materials-based homogeneous transistor-memory architecture for neuromorphic hardware," *Science*, vol. 373, no. 6561, pp. 1353–1358, Sep. 2021, doi: 10.1126/science.abg3161.
- [4] R. Yang et al., "Ternary content-addressable memory with MoS₂ transistors for massively parallel data search," *Nature Electron.*, vol. 2, no. 3, pp. 108–114, Mar. 2019, doi: 10.1038/s41928-019-0220-7.
- [5] K. Ni et al., "Ferroelectric ternary content-addressable memory for one-shot learning," *Nature Electron.*, vol. 2, no. 11, pp. 521–529, Nov. 2019, doi: 10.1038/s41928-019-0321-3.
- [6] X. Zhang, M. Ezawa, and Y. Zhou, "Magnetic skyrmion logic gates: Conversion, duplication and merging of skyrmions," *Sci. Rep.*, vol. 5, no. 1, p. 9400, Mar. 2015, doi: 10.1038/srep09400.
- [7] R. Tomasello, E. Martinez, R. Zivieri, L. Torres, M. Carpentieri, and G. Finocchio, "A strategy for the design of skyrmion racetrack memories," *Sci. Rep.*, vol. 4, no. 1, p. 6784, Oct. 2014, doi: 10.1038/srep06784.
- [8] S. Li et al., "Magnetic skyrmions for unconventional computing," Mater. Horizons, vol. 8, no. 3, pp. 854–868, 2021, doi: 10.1039/ D0MH01603A.
- [9] Z. He and D. Fan, "A tunable magnetic skyrmion neuron cluster for energy efficient artificial neural network," in *Proc. Design, Autom. Test Eur. Conf. Exhib. (DATE)*, Mar. 2017, pp. 350–355.
- [10] S. Li, W. Kang, Y. Huang, X. Zhang, Y. Zhou, and W. Zhao, "Magnetic skyrmion-based artificial neuron device," *Nanotechnology*, vol. 28, no. 31, Jul. 2017, Art. no. 31LT01, doi: 10.1088/1361-6528/aa7af5.
- [11] G. Panagopoulos, C. Augustine, and K. Roy, "A framework for simulating hybrid MTJ/CMOS circuits: Atoms to system approach," in *Proc. Design, Autom. Test Eur. Conf. Exhib. (DATE)*, Mar. 2012, pp. 1443–1446.
- [12] L. Gnoli and F. Riente, "A skyrmion content-addressable cell for skyrmion magnetic memories," *Nanotechnology*, vol. 33, no. 20, Feb. 2022, Art. no. 205203, doi: 10.1088/1361-6528/ ac4dc2.
- [13] M. J. Donahue and M. Donahue, "OOMMF user's guide, version 1.0," Nat. Inst. Standards Technol., Gaithersburg, MD, USA, Interagency Rep. NISTIR 6376, 1999.

- [14] J. Xiao, A. Zangwill, and M. D. Stiles, "Boltzmann test of Slonczewski's theory of spin-transfer torque," *Phys. Rev. B, Condens. Matter*, vol. 70, no. 17, Nov. 2004, Art. no. 172405, doi: 10.1103/PhysRevB.70.172405.
- [15] A. Manchon et al., "Current-induced spin-orbit torques in ferromagnetic and antiferromagnetic systems," Rev. Mod. Phys., vol. 91, no. 3, Sep. 2019, Art. no. 035004, doi: 10.1103/RevModPhys.91.035004.
- [16] S. Rohart and A. Thiaville, "Skyrmion confinement in ultrathin film nanostructures in the presence of dzyaloshinskii–moriya interaction," *Phys. Rev. B, Condens. Matter*, vol. 88, Nov 2013, Art. no. 184422, doi: 10.1103/PhysRevB.88.184422.
- [17] P. J. Metaxas et al., "Creep and flow regimes of magnetic domain-wall motion in ultrathin Pt/Co/Pt films with perpendicular anisotropy," Phys. Rev. Lett., vol. 99, no. 21, Nov. 2007, Art. no. 217208, doi: 10.1103/PhysRevLett.99.217208.
- [18] L. Zhu, D. C. Ralph, and R. A. Buhrman, "Maximizing spin-orbit torque generated by the spin Hall effect of Pt," *Appl. Phys. Rev.*, vol. 8, no. 3, Sep. 2021, Art. no. 031308, doi: 10.1063/5.0059171.
- [19] J. Sampaio, V. Cros, S. Rohart, A. Thiaville, and A. Fert, "Nucleation, stability and current-induced motion of isolated magnetic skyrmions in nanostructures," *Nature Nanotechnol.*, vol. 8, no. 11, pp. 839–844, Nov. 2013, doi: 10.1038/nnano.2013.210.
- [20] F. Jonietz et al., "Spin transfer torques in MnSi at ultralow current densities," *Science*, vol. 330, no. 6011, pp. 1648–1651, Dec. 2010, doi: 10.1126/science.1195709.
- [21] M. G. Mankalale, Z. Zhao, J. Wang, and S. S. Sapatnekar, "SkyLogic—A proposal for a skyrmion-based logic device," *IEEE Trans. Electron Devices*, vol. 66, no. 4, pp. 1990–1996, Apr. 2019.
- [22] P. Kumar, S. Narla, Y.-C. Liao, and A. Naeemi, "Crosslayer modeling and design for spin-orbit-torque and magnetoelectric memory arrays and compute-in-memory," *Proc. SPIE*, vol. 12205, Oct. 2022, Art. no. 1220504, doi: 10.1117/12.2633519.
- [23] X. Yin, K. Ni, D. Reis, S. Datta, M. Niemier, and X. S. Hu, "An ultradense 2FeFET TCAM design based on a multi-domain FeFET model," *IEEE Trans. Circuits Syst. II, Exp. Briefs*, vol. 66, no. 9, pp. 1577–1581, Sep. 2019.
- [24] W. Zhao and Y. Cao. (2008). Predictive Technology Model (PTM). [Online]. Available: http://ptm.asu.edu
- [25] S. Matsunaga, A. Katsumata, M. Natsui, T. Endoh, H. Ohno, and T. Hanyu, "Design of a nine-transistor/two-magnetic-tunnel-junctioncell-based low-energy nonvolatile ternary content-addressable memory," *Jpn. J. Appl. Phys.*, vol. 51, no. 2S, Feb. 2012, Art. no. 02BM06, doi: 10.1143/jjap.51.02bm06.
- [26] C. Wang, D. Zhang, L. Zeng, E. Deng, J. Chen, and W. Zhao, "A novel MTJ-based non-volatile ternary content-addressable memory for high-speed, low-power, and high-reliable search operation," *IEEE Trans. Circuits Syst. I, Reg. Papers*, vol. 66, no. 4, pp. 1454–1464, Apr. 2019.
- [27] L. Zheng, S. Shin, S. Lloyd, M. Gokhale, K. Kim, and S. M. Kang, "RRAM-based TCAMs for pattern search," in *Proc. IEEE Int. Symp. Circuits Syst. (ISCAS)*, May 2016, pp. 1382–1385.
- [28] X. Fong and K. Roy, "Low-power robust complementary polarizer STT-MRAM (CPSTT) for on-chip caches," in 5th IEEE Int. Memory Workshop, Monterey, CA, USA, 2013, pp. 88–91, doi: 10.1109/IMW.2013.6582105.
- [29] R. Gruber et al., "Skyrmion pinning energetics in thin film systems," *Nature Commun.*, vol. 13, no. 1, p. 3144, Jun. 2022, doi: 10.1038/s41467-022-30743-4.